Journal of Materials Chemistry A

Accepted Manuscript

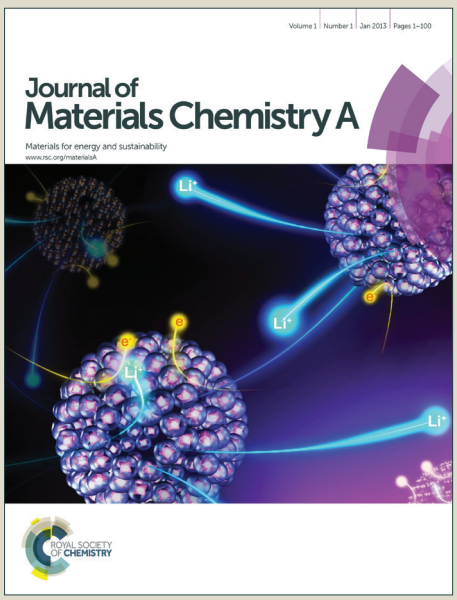

ROYAL SOCIETY OF CHEMISTRY

www.rsc.org/materialsA

Journal Name

RSCPublishing

ARTICLE

Hollow Zeolite encapsulated Ni-Pt bimetals for sintering and coking resistant dry reforming of methane

Cite this: DOI: 10.1039/x0xx00000x

Received 00th January 2012,
Accepted 00th January 2012

DOI: 10.1039/x0xx00000x

www.rsc.org/

Chengyi Dai,[a] Shaohua Zhang,[b] Anfeng Zhang,[a] Chunshan Song,[a,c]* Chuan Shi [b]* and Xinwen Guo[a]*

Highly dispersed Ni-Pt bimetallic nanoparticles encapsulated in hollow silicalite-1 single crystals (1.5Ni-0.5Pt@Hol S-1) were a superior catalyst for sintering and coking resistant dry (CO_2) reforming of CH_4. Large Ni particles loaded on the surface of solid silicalite-1 crystals triggered coke formation, which simultaneously degraded the catalytic activity of small Ni particles. With Ni encapsulated in hollow crystals, the small Ni particles inhibit coke formation. The encapsulating shell prevents coke formed outside from degrading the activity of nickel on the inside, leading to stable high activity even in the presence of carbon. Compared with single metal (Ni or Pt), 1.5Ni-0.5Pt@Hol S-1 enhances the dispersion of nickel and platinum. In the dry reforming of methane, the 1.5Ni-0.5Pt@Hol S-1 catalyst operated stably under high gaseous hourly space velocity (GHSV=72000 $mLg^{-1}h^{-1}$) without any inert gas. Only 1.0 wt% carbon deposition was observed by thermogravimetric analysis (TGA) after 6 h the reaction. Hollow zeolite crystals can reliably support coke resistant catalysts for dry reforming of CH_4 and multi-metallic catalysts with well-dispersed nanoparticles.

1 Introduction

Dry (CO_2) reforming of methane (DRM) is a well-studied reaction that is of both scientific and industrial importance because it could transformed greenhouse gasses (CH_4 and CO_2) into the energy carrier synthesis gas (CO and H_2), which can be converted to valuable chemicals via the Fischer-Tropsch reaction.[1-3] In addition, its endothermic property makes DRM a promising method for energy storage and energy transfer. It can be used in energy transfer from solar energy to chemical energy, energy storage in the form of CO and H_2, and transporting nuclear energy.[4-6] For DRM, Ni-based catalysts have been regarded as the most promising because of their high activity, low cost and extensive supply.[7-14] According to previous studies, the sintering of Ni particles and carbon deposition under high reaction temperature (typically 800 °C) proved to be the main impediments for stable catalytic performance.[15-17] Therefore, preventing Ni sintering, decreasing the carbon deposition or reducing the effect of carbon deposition on the catalyst are very important for industrial progress of DRM.

Various methods to prevent Ni sintering or reduce coke formation have been investigated, including reducing the particle size,[18, 19] using a promoter,[20-25] and using a support,[26-30] among others. These methods include preparing highly dispersed Ni supported on molecular sieve which has large surface area and pore volume,[31] modifying the properties of support with basic alkaline and rare earth metals, as well as designing catalysts with certain structures like core/shell structure, alloy and hydrotalcite.[32-36] These methods successfully prepared catalysts with good dispersion of Ni metal and high carbon resistance.

In recent years, metal@oxide core shell structure nanoparticles have demonstrated good properties in the DRM, which can significantly resist coke formation.[37, 38] Sibudjing Kawi et al. reported that Ni-yolk@Ni@SiO_2 with 11.2 nm silica shell thickness shows more stable than Ni@SiO_2 at 800 °C. The authors argue that the dual effects of formation of small satellite Ni particles due to strong Ni-SiO_2 interactions and yolk shell structures contribute to its high activity and stability. The nanostructures of silica-encapsulated NiO nanoparticles (NPs) doped with La, Ce, Ba, Co, Cu, and Fe were prepared by Weijie Ji.[37] Due to the distribution uniformly and strong alkalinity, the La-doped Ni@SiO_2 catalyst is superior to those doped with other elements in the partial oxidation of methane. Fornasiero et al. also found that an embedded Rh@Al_2O_3 catalyst was more resistant to deactivation than the Rh/Al_2O_3 POM.[39] However, using these methods, the metallic particles are often large and the pores in the shell are often difficult to control, which is not conducive to the catalytic activity. Furthermore, metal@silica core shell nanoparticle studies have mainly focused on the

prevention of carbon deposition or metal sintering. The potential to retain catalyst activity in the presence of coke has not been reported.

In the past years, zeolites as supports have attracted interest due to their unique properties (e.g., high thermal stability, regular microporosity, and unique shape selectivity) which can be widely applied in catalytic operations.[40-42] Hollow zeolites have attracted considerable interest because of their superior performance in the selectivity of product, anti-leaching of active site and anti-sintering of metal.[43-48] The ability of hollow zeolite encapsulated metals to resist coke formation has not been previously reported. Herein, we report the encapsulation of Ni-Pt bimetals in hollow silicalite-1 single crystals for the first time. This material exhibits excellent metal dispersion and superior catalytic performance for sintering and coking resistant CO_2 reforming of CH_4. In addition, we report, also for the first time, a protective effect of the zeolite shell in the hollow crystals to allow continued catalytic activity in the presence of carbon.

2 Experimental

2.1 Preparation of silicalite-1 zeolite

Silicalite-1 (S-1) was synthesized with the clear solution method. Typically, 15.4 ml of tetraethyl orthosilicate (TEOS) was mixed with a certain amount of TPAOH solution. The molar composition of the synthesis mixture was 1 TEOS: 0.27 TPAOH: 37 H_2O. After being stirred for 3 h at 35 ^oC, the solution was heated at 80 ^oC to remove the ethanol generated during the hydrolysis of TEOS and then water was added to maintain constant volume. After crystallization at 170 ^oC for 3 days, the product was recovered by centrifugation and dried overnight at 100 ^oC. Finally, the template was removed by calcination in static air at 540 ^oC for 6 h.

2.2 Preparation of Ni@Hol S-1, Pt@Hol S-1 and Ni-Pt@Hol S-1

NiO/S-1 was synthesized by an incipient-wetness impregnation method. In brief, the calcined silicalite-1 was impregnated with an aqueous solution of $NiCl_2$; after drying overnight at 100 ^oC, the product was calcined in static air at 400 ^oC for 2 h. The ideal Ni loading on the NiO/S-1 were 1.5, 3 and 5 wt%, respectively. The resulting samples were denoted as 1.5NiO/S-1, 3NiO/S-1 and 5NiO/S-1, respectively.

The as-prepared NiO/S-1 was treated with 0.3 M TPAOH (20 ml of solution per gram of zeolite) at 170 ^oC for 72 h, then dried overnight at 100 ^oC and calcined in static air at 400 ^oC for 2 h to obtain NiO@Hol S-1. The resulting samples were denoted as 1.5NiO@Hol S-1, 3NiO@Hol S-1 and 5NiO@Hol S-1, respectively.

Pt/S-1 was prepared by the same method as NiO/S-1, using H_2PtCl_6 as the Pt source. The ideal platinum loading on Pt/S-1 was 0.5 wt%. After treatment with 0.3 M TPAOH (20 ml of solution per gram of zeolite) at 170 ^oC for 72 h, drying overnight at 100 ^oC and calcining in static air at 400 ^oC for 2 h, the Pt@Hol S-1 was obtained. The resulting sample was denoted as 0.5Pt@Hol S-1.

Bimetals encapsulated in the hollow S-1 were prepared by similar methods as the single metals. $NiCl_2$ and H_2PtCl_6 were used as the Ni and Pt sources, and a co-impregnation method was used to synthesize bimetals/S-1. The ideal nickel loading on the S-1 were 1.5 wt%, while the ideal platinum loading on the S-1 were 0.1, 0.3 and 0.5 wt%, respectively. The as-prepared NiO-Pt/S-1 was treated with 0.3 M TPAOH (20 ml of solution per gram of zeolite) at 170 ^oC for 72 h, then dried overnight at 100 ^oC and calcined in static air at 400 ^oC for 2 h to obtain NiO-Pt@Hollow S-1. The resulting samples were denoted as 1.5NiO-0.1Pt@Hol S-1, 1.5NiO-0.3Pt@Hol S-1 and 1.5NiO-0.5Pt@Hol S-1, respectively.

The real Ni and Pt loading on the samples are listed in Table 1 and Table S2, as measured by inductively coupled plasma (ICP) mass spectrometry. After reduction under hydrogen at 800 °C for 30 min, xNi@Hol S-1, 0.5Pt@Hol S-1 and 1.5Ni-yPt@Hol S-1 were obtained, where x (1.5, 3 and 5) and y (0.1, 0.3 and 0.5) represent the ideal mass percentage content of Ni and Pt, respectively,

2.3 Characterization

Powder X-ray diffraction (XRD) patterns were recorded on a Rigaku Smartlab diffractometer using a nickel-filtered CuKa X-ray source at a scanning rate of 0.02^o over the range between 5° and 80°.

Transmission electron microscopy (TEM) images were taken on a Tecnai G2 20 S-twin instrument (FEI Company) with an acceleration voltage of 200 kV. The samples for TEM analysis were prepared by dipping the carbon-coated copper grids into the ethanol solutions of the samples and drying at ambient condition.

Ar isotherms were measured with a Quantachrome autosorb-iQ2 gas adsorption analyzer at -186 ^oC. Prior to the measurement, the samples were degassed in vacuum at 300 ^oC for 10 h. The Brunauer-Emmett-Teller (BET) method was applied to calculate the total surface area (S_{BET}), while the t-plot method was used to discriminate between micro- and mesoporosity. In the t-plot, the reported mesopore surface area (S_{meso}) consists of contributions from the outer surface of the particles as well as mesopores and macropores.

Scanning electron microscopy (SEM) images were obtained on a Hitachi S-5500 instrument with an acceleration voltage of 3 kV. Some samples were sputtered with a thin film of gold.

The solid state NMR spectra were measured on a Bruker Avance III 600 spectrometer equipped with a 14.1 T wide-bore magnet using a 4 mm MAS probe.

Fourier transform infrared (FI-IR) spectra were taken on EQUINOX55 FT-IR spectrometer with a resolution of 4 cm^{-1}.

The elemental analysis of catalysts was carried out on a Perkin Elmer OPTIMA 2000DV ICP Optical Emission Spectrometer.

Thermogravimetric analysis (TGA) was performed on an SDT Q600 (TA Instruments, USA) in the temperature range of 25-800 °C under air at a heating rate of 10 °C min^{-1}.

H_2-TPR measurements were carried out with a ChemBET Pulsar TPR/TPD instrument (Quantachrome, USA) to analyze the reducibility of the calcined catalysts. Prior to the reduction, the calcined sample (0.10 g) was placed in a quartz tube reactor in the interior of a controlled oven. The sample was flushed with high purity argon at 300 °C for 1 h to remove water and other contaminants then cooled to room temperature. A gas mixture containing 5 vol% H_2 in Ar was passed through the sample at a total flow rate of 30 ml min^{-1}. The temperature and detector signals were then continuously recorded while heating at 10 °C min^{-1} up to 900 °C. A cooling trap was also placed between the sample and the detector for removal of released water formed during the reduction process.

2.4 Catalytic tests

The dry reforming reaction of methane was carried out in a quartz glass fixed-bed reactor at 800 °C and atmospheric pressure with a total flow rate of 240 ml/min of mixed gasses of CH_4:CO_2=1:1. A total of 200 mg of the catalyst was put inside the reactor. Before reaction, the catalyst was reduced at 500 °C for 1 h followed by introduction of CO_2 and CH_4. The composition of the product gases was analyzed with an on-line gas chromatograph equipped with a thermal conductivity detector.

3 Results and discussion

3.1. Material synthesis and characterization

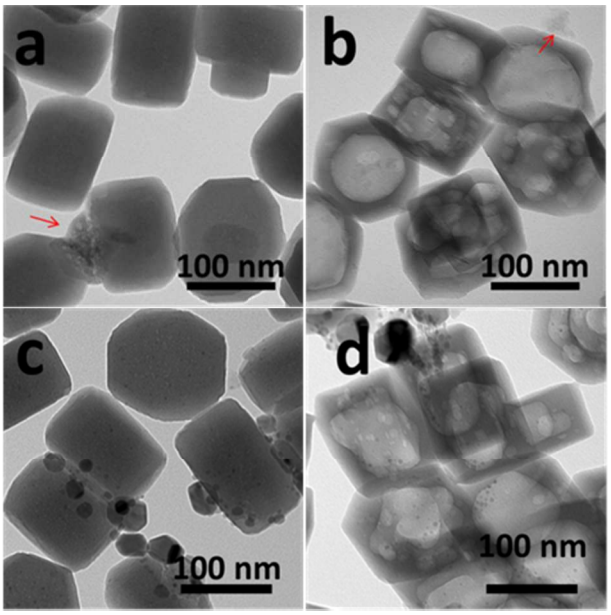

Fig. 1. TEM images of prepared (a, c) 1.5NiO/S-1 and (b, d) 1.5NiO@Hol S-1 after calcination at 400 °C for 2 h (a, b) and reduction under H_2 at 800 °C for 30 min (c, d).

Fig. 1a shows a TEM image of prepared 1.5NiO/S-1 after calcination at 400 °C for 2 h. Nickel oxide species are not uniformly distributed, instead presenting large particles on the surface of the crystals. After TPAOH treatment, large voids were formed in the silicalite-1 crystals by controlled silicon leaching with OH^- and thin intact shells were formed by the re-crystallization of silicon on the crystal surface with TPA^+. In this process, nickel in the micropores or small particles on the crystal surfaces become encapsulated in the voids of hollow crystals. Large Ni particles instead fall down from the surface during the "dissolution-recrystallization" process and remain on the hollow crystal surfaces (Fig. 1b). After 1.5NiO/S-1 reduction under H_2 at 800 °C for 30 min, a bimodal distribution of Ni particles formed on the crystals with 15.0 and 3.13 nm average diameters (Table 1, Fig 1c). The bimodal distribution occurred due to weak and strong interactions between the Ni species and support. Nickel encapsulated in the zeolite hollow crystals (Fig. 1d) were well dispersed with a 3.44 nm average particle diameter, but there are also nickel particles on the outer surface of crystals, which grow to 14.6 nm in average diameter during the reduction process.

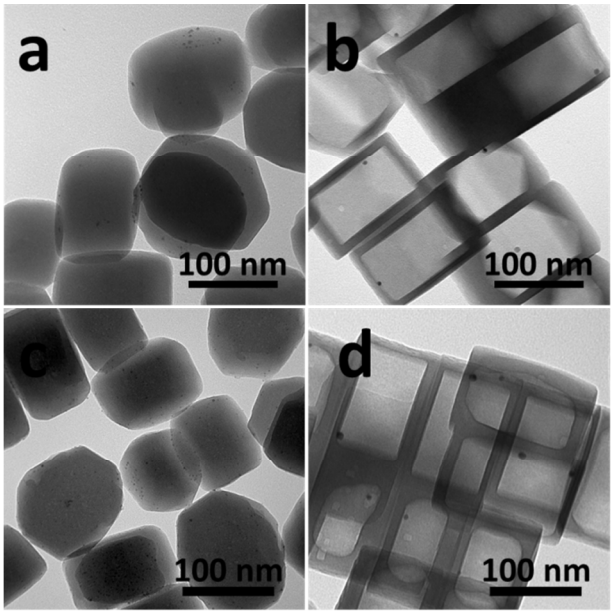

Fig. 2. TEM images of prepared (a, c) 0.5Pt/S-1 and (b, d) 0.5Pt@Hol S-1 after calcination at 400 °C for 2 h (a, b) and reduction under H_2 at 800 °C for 30 min (c, d).

Fig. 2a shows a typical TEM image of the prepared 0.5Pt/S-1, which clearly exhibits those platinum nanoparticles, with 1.81 nm diameter, are located on the surface of the crystals. After TPAOH treatment, almost all the platinum particles were encapsulated in the hollow crystals (Fig. 2b). However, the ICP results show only 0.227 wt% Pt in the sample, indicating that about half of the platinum was lost in the TPAOH treatment process due to the weak interaction between platinum and the support. Furthermore, the encapsulated platinum tended to agglomerate into particles of 5.21 nm in size, about 3 times larger than that of 0.5Pt/S-1, which is not conducive to high utilization in a platinum-catalyzed reaction. After reduction under H_2 at 800 °C, the Pt particle sizes on the solid or in the hollow crystals increased slightly, to 2.24 and 6.31 nm, respectively (Fig. 2c, d).

Fig. 3a shows a typical TEM image of the prepared 1.5NiO-0.5Pt/S-1. Contrary to samples of 1.5NiO/S-1 and 0.5Pt/S-1, there are no observable particles on the surface of crystals. This is attributed to a high dispersion of nickel and platinum. After TPAOH treatment, several particles with average size of 3.14 nm were encapsulated in the hollow crystals (Fig. 3b). These NiO-Pt particles are smaller than the encapsulated Pt particles (Fig. 2b). The amount of platinum in 1.5NiO-0.5Pt@Hol S-1 is larger than that of 0.5Pt@Hol S-1, confirming that the presence of nickel significantly inhibited aggregation and loss of platinum. After 1.5NiO-0.5Pt/S-1 reduction under H_2 at 800 °C, the average size of Ni-Pt bimetallic particles was 4.40 nm and there were no sintered nickel particles on the crystals (Fig. 3c). The presence of platinum significantly inhibited sintering of nickel. After H_2 reaction, Ni-Pt bimetallic particles encapsulated in the hollow crystals maintained a high dispersion (4.57 nm average size, Fig. 3d). According to EDX analysis, each particle contains both nickel and platinum elements, demonstrating an interaction between nickel and platinum is involved in motivation their high dispersion in the hollow crystal.

The ^{29}Si NMR spectra (Fig. S4) of 1.5NiO/S-1 and 1.5NiO@Hol S-1 show three major peaks at ca. -105 ppm (Q^2), ca. -114 ppm (Q^3) and ca. -117 ppm (Q^4). After TPAOH treatment, the fractions of Q^2 and Q^3 increased to 7% and 67%, respectively, while the fraction of Q^4 decreased to 26%. These trends result from an increase of silanols, which could enhance the interaction between nickel and support as well as improve the metal particles deposition. Fig. S5 shows the FT-IR spectra in the hydroxyl range of the 1.5NiO/S-1 and 1.5NiO@Hol S-1. The peak 3740, 3730 and 3500 cm^{-1} correspond to vibrations of Si-OH on external surfaces of crystals, free Si-OH in defects and Si-OH in defects bonded by hydrogen bonding to framework oxygen in "hydroxyl nests", respectively.[49] The treatment of silicalite-1 with TPAOH enhance the bands corresponding to Si-OH and Si-OH…O in defects and "hydroxyl nests" (3730 and 3500 cm^{-1}), which in agreement with the results of ^{29}Si MAS NMR. The FT-IR spectra of the samples (Fig. S6) also show the characteristic absorption peak of the silicalite-1 at 1230, 1100, 800, 550 and 450 cm^{-1}, respectively. Because of the small content of Ni and the strong background absorption peak of silicalite-1, the nickel silicate structure absorption peaks of 1.5NiO/S-1 and 1.5NiO@Hol S-1 samples are not clearly apparent.

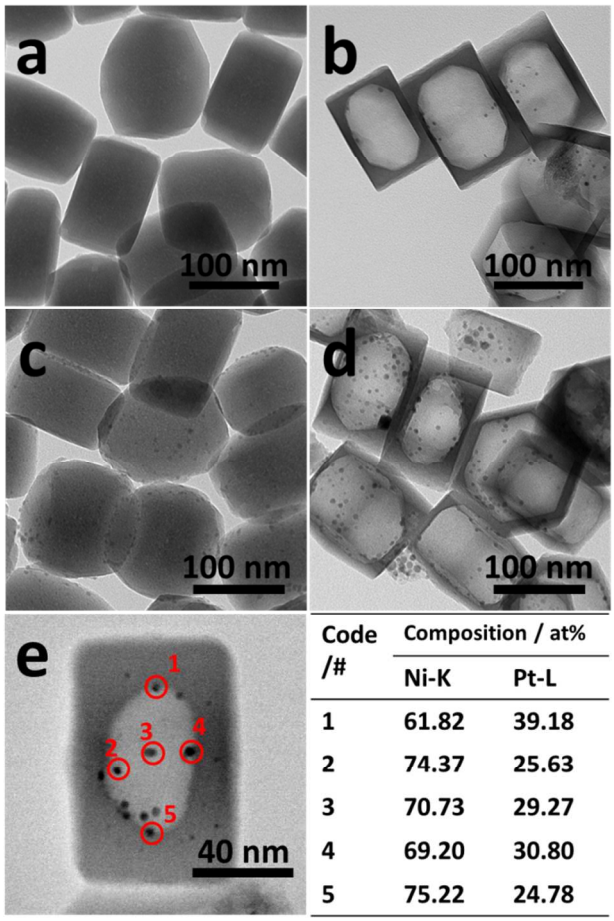

Code /#	Composition / at%	
	Ni-K	Pt-L
1	61.82	39.18
2	74.37	25.63
3	70.73	29.27
4	69.20	30.80
5	75.22	24.78

Fig. 3. TEM images of prepared (a, c) 1.5NiO-0.5Pt/S-1 and (b, d) 1.5NiO-0.5Pt@Hol S-1 after calcination in air at 400 °C for 2 h (a, b) and reduction under H_2 at 800 °C for 30 min (c, d). (e) STEM image of prepared 1.5NiO-0.5Pt@Hol S-1 after reduction under H_2 at 800 °C for 30 min, and quantified phase compositions in the Ni-Pd nanoparticles from STEM maps

Table 1. Composition and average metal particle size in the various samples after calcination in air at 400 °C for 2 h and reduction under H_2 at 800 °C for 30 min, the metal particle size distributions of prepared samples are shown in Fig. S1-3.

Sample Code	Resulting composition[a]		Average particle size[b] (nm)	Average particle size [c] (nm)
	Ni (wt%)	Pt (wt%)		
1.5NiO/S-1	1.53	/	/	3.13 (15.0[d])
1.5NiO@Hol S-1	1.96	/	/	3.44 (14.6[d])
0.5Pt/S-1	/	0.487	1.81	2.24
0.5Pt@Hol S-1	/	0.227	5.21	6.31
1.5NiO-0.5Pt/S-1	1.51	0.525	/	4.40
1.5NiO-0.5Pt@Hol S-1	1.58	0.540	3.14	4.57

[a]ICP analysis, [b]samples after calcination in air at 400 °C for 2 h, [c]samples after reduction under H_2 at 800 °C for 30 min, [d]average size of large particles.

Table 2. Textual properties of 1.5NiO/S-1, 1.5NiO@Hol S-1, 0.5Pt/S-1, 0.5Pt@Hol S-1, 1.5NiO-0.5Pt/S-1 and 1.5NiO-0.5Pt@Hol S-1 after calcination in air at 400 °C for 2 h.

Sample Code	S_{micro}[a] [m^2g^{-1}]	S_{meso}[a] [m^2g^{-1}]	S_{BET}[b] [m^2g^{-1}]	V_{micro}[a] [cm^3g^{-1}]	V_{pore}[c] [cm^3g^{-1}]
1.5NiO/S-1	378	98	476	0.15	0.53
1.5NiO@Hol S-1	311	125	436	0.12	0.86
0.5Pt/S-1	388	95	483	0.15	0.53
0.5Pt@Hol S-1	326	120	446	0.13	0.77
1.5NiO-0.5Pt/S-1	374	95	469	0.15	0.51
1.5NiO-0.5Pt@Hol S-1	313	117	430	0.12	0.94

[a] t-plot method [b] BET method [c] p/p_0=0.99.

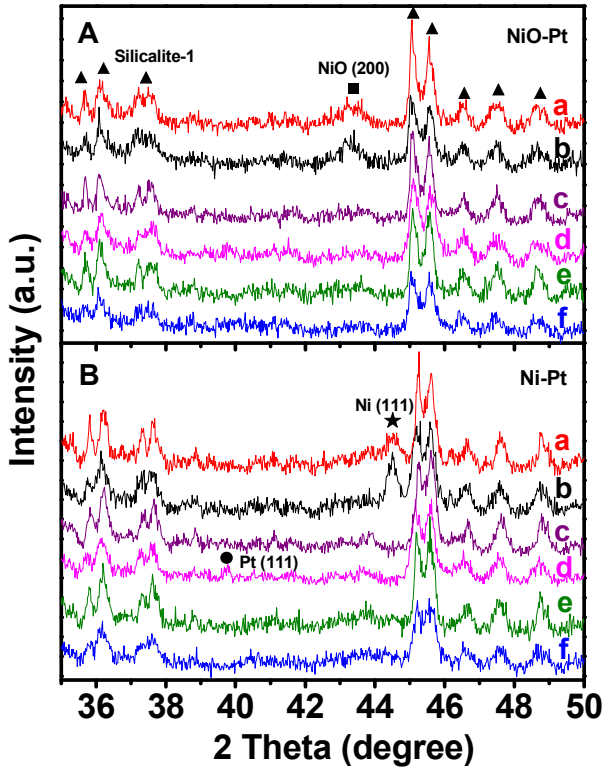

Fig. 4. XRD patterns of prepared (a) 1.5NiO/S-1, (b) 1.5NiO@Hol S-1, (c) 0.5Pt/S-1, (d) 0.5Pt@Hol S-1, (e) 1.5NiO-0.5Pt/S-1, (f) 1.5NiO-0.5Pt@Hol S-1 after calcination in air at 400 °C for 2 h (A) and reduction under H_2 at 800 °C for 30 min (B).

The high dispersion of Ni(O)-Pt bimetallics in hollow crystals is also demonstrated by the XRD patterns. Besides the strong diffraction peaks of MFI topology (Fig. S7), several new peaks appear between 35° and 50°, shown in Fig. 4. After calcination in air at 400 °C, for 1.5NiO/S-1 and 1.5NiO@Hol S-1, the XRD patterns exhibited the characteristic diffraction peaks of NiO at 2θ=43.1° (JCPDS no. 65-2901). However, the diffraction peak of NiO in the 1.5NiO-0.5Pt@Hol S-1 became broad, which suggests the particles in the hollow crystals are smaller. Fig. 4B shows the XRD patterns of the samples after reduction under H_2 at 800 °C. As expected, the XRD patterns exhibited the characteristic diffraction peaks of Ni at 2θ=44.5° (JCPDS no. 65-2865) in the samples of 1.5NiO/S-1 and 1.5NiO@S-1 as well as the peak of Pt at 2θ=39.8° (JCPDS no. 04-0802) in the sample of 0.5Pt@S-1. The broader peaks observed for Ni and Pt in the sample of 1.5NiO-0.5Pt@S-1 indicate their high dispersion in the hollow crystals after reduction at 800 °C. XRD results are consistent with the TEM results (Fig. 1-3).

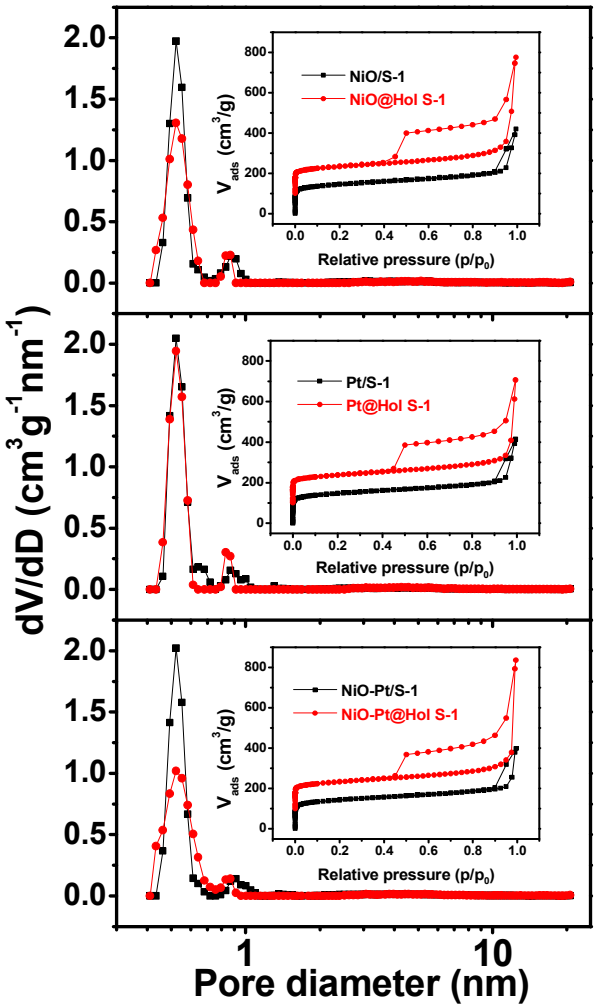

Fig. 5. Ar adsorption and desorption isotherms at 87 K (inset) and pore size distributions of 1.5NiO/S-1, 1.5NiO@Hol S-1, 0.5Pt/S-1, 0.5Pt@Hol S-1, 1.5NiO-0.5Pt/S-1 and 1.5NiO-0.5Pt@Hol S-1 after calcination in air at 400 °C for 2 h. The

isotherms of hollow samples are offset by 100 cm^3g^{-1}. The pore size distributions were determined by non-local density functional theory (NLDFT).

Fig. 5 shows Ar adsorption and desorption isotherms at -186 °C (inset) and pore size distributions of the samples after calcination in air at 400 °C for 2 h. The Ar adsorption-desorption isotherms of metal encapsulated hollow crystals show an H2 hysteresis loop with an abrupt step around p/p_0=0.45 in the desorption branch. This shows that, during the TPAOH treatment, the hollow structure of the zeolite is preserved, which is consistent with the TEM results. The micropore size distributions derived from the argon adsorption isotherms indeed confirm that the original micropore size is not affected during the alkaline treatment. Table 2 lists textual properties of the samples after calcination in air at 400 °C for 2 h. Compared with solid crystals, the micropore surface areas and volumes of hollow crystals decrease after TPAOH treatment, while the mesopore surface areas and total pore volumes increase.

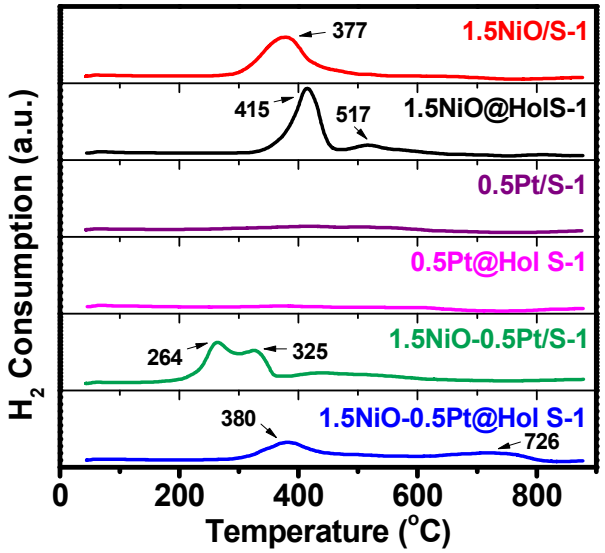

Fig. 6. H_2-TPR profiles of 1.5NiO/S-1, 1.5NiO@Hol S-1, 0.5Pt/S-1, 0.5Pt@Hol S-1, 1.5NiO-0.5Pt/S-1 and 1.5NiO-0.5Pt@Hol S-1

To gain a better understanding of the interaction between nickel, platinum and support, H_2-TPR experiments were conducted, as shown in Fig. 6 and Table S1. Ni^{2+} is directly reduced to Ni^0 without any intermediate oxidation state species.[50] There are no peaks for platinum-containing samples (0.5Pt/S-1 and 0.5Pt@Hol S-1) due to its high degree of reduction and low content. Differences in H_2 consumption peaks can be attributed to various NiO species. From the TPR profiles, 1.5NiO/S-1 exhibits a single broad reduction peak in the range of 300-450 °C. For 1.5NiO@Hol S-1, the reaction temperature increases to 330-470 °C with a second smaller peak around 517 °C, suggesting that the nickel-support interaction is strengthened during the encapsulating process. The introduction of platinum can significantly decrease the nickel oxide reduction temperature due to the hydrogen spillover effect. For 1.5NiO-0.5Pt/S-1, the reduction peaks centered at 264 and 325 °C can be attributed to NiO species with different interactions with platinum. For 1.5NiO-0.5Pt@Hol S-1, the low temperature reduction peak transforms into a broad peak and moves to higher temperature. In addition, a higher reduction peak around 726 °C suggests a stronger interaction between metal and support, which is conducive to improving the catalytic performance in the reforming process.[38, 51]

3.2 Catalytic performance and carbon resistance

The activity and stability of catalysts during dry reforming of methane were tested under a high gas hourly space velocity (GHSV=72000 $mLg^{-1}h^{-1}$) and without any inert gas. Fig. 7 illustrates the conversion versus time on stream for the various catalyst cycles. For 1.5Ni/S-1, the initial conversion of CO_2 and CH_4 were 76 and 73 %, respectively. However, conversion rapidly decreased to zero within one hour. 1.5Ni-0.5Pt/S-1 had similar initial activity as 1.5Ni/S-1, however, the introduction of platinum enhanced the stability of the catalyst. 1.5Ni-0.5Pt/S-1 deactivated within 6 hours. The encapsulated Ni-based catalysts showed the best catalytic performance, with conversion of CO_2 and CH_4 maintained with little deactivation past 6 hours of time on stream. The initial activities of 1.5Ni@Hol S-1 and 1.5Ni-0.5Pt@Hol S-1 were almost the same, but the 1.5Ni-0.5Pt@Hol S-1 showed better stability compared to that of 1.5Ni@Hol S-1. After 20 h reaction, both CH_4 and CO_2 conversions were higher than 60% over 1.5Ni-0.5Pt@Hol S-1, but lower than 30% over 1.5Ni@Hol S-1 (Fig. S12).

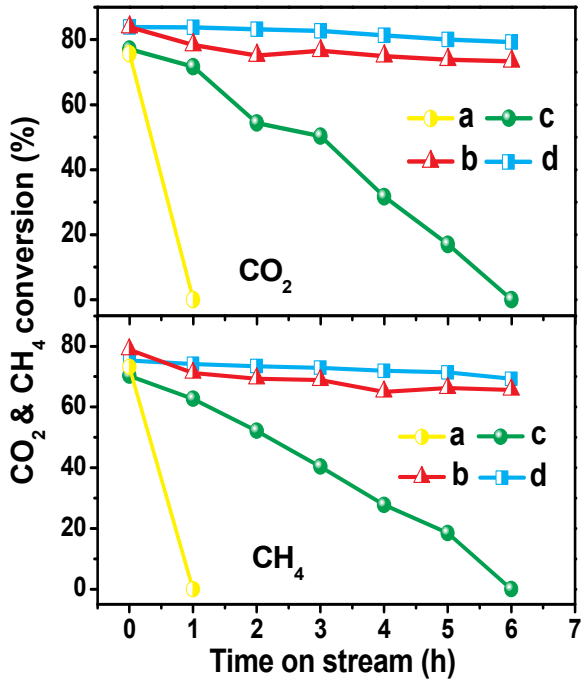

Fig. 7. CO_2 and CH_4 conversion as a function of time on stream over (a) 1.5Ni/S-1, (b) 1.5Ni@Hol S-1, (c) 1.5Ni-0.5Pt/S-1, and (d) 1.5Ni-0.5Pt@Hol S-1 catalysts [800 °C, atmospheric pressure, GHSV=72000 $mLg^{-1}h^{-1}$, and CH_4/CO_2=1:1(v/v)]

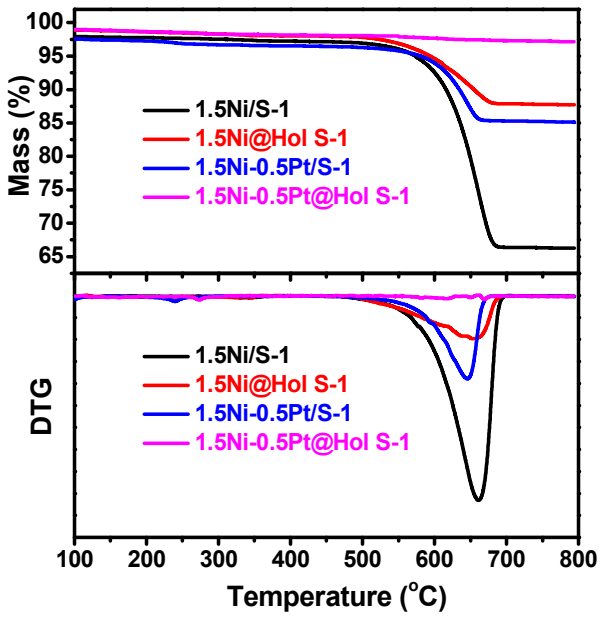

Fig. 8. TG and DTG curves of spent catalysts after stability tests; the reaction time was 1 h for 1.5Ni/S-1 and 6 h for the other three catalysts.

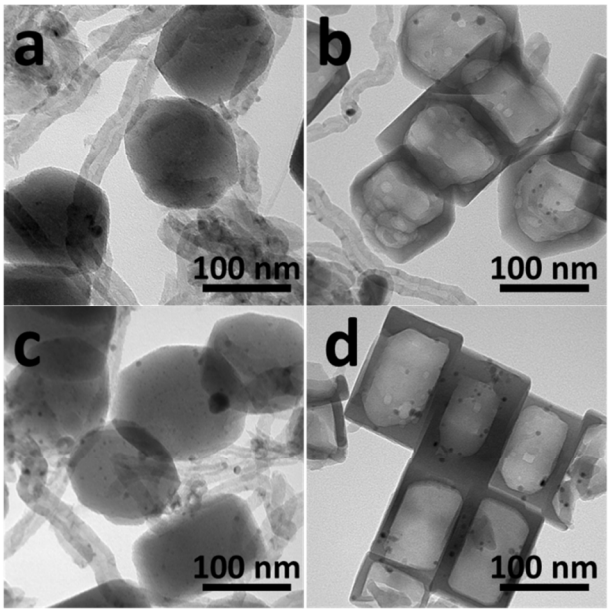

Fig. 9. TEM images of the spent catalysts, (a) 1.5Ni/S-1, (b) 1.5Ni@Hol S-1, (c) 1.5Ni-0.5Pt/S-1, (d) 1.5Ni-0.5Pt@Hol S-1, the reaction time was 1 h for 1.5Ni/S-1 and 6 h for the other three catalysts.

The amounts of the deposited carbon were investigated by thermal gravimetric (TG) and differential thermal gravimetric (DTG) experiments (Fig. 8). No peak was observed in the DTG curves for the 1.5Ni-0.5Pt@Hol S-1 catalyst, whereas peaks appear in the temperature range of 500-700 °C for the other three catalysts. The peak in this temperature range implies the formation of crystalline carbons, such as filamentous or graphitic carbon.[52-55] Except for the loss of adsorbed water, the weight loss of spent 1.5Ni-0.5Pt@Hol S-1 is only 1.0 %, while the weight loss of spent 1.5Ni-0.5Pt/S-1 and 1.5Ni@Hol S-1 are 11.4 and 10.3 %, respectively. The fastest coke deposition occurs on the 1.5Ni/S-1 catalyst, with a 31.0 % weight loss measured in DTG.

Although 1.5Ni-0.5Pt/S-1 and 1.5Ni@Hol S-1 have a similar amount of carbon deposition, their catalytic stabilities are very different, as shown in Fig. 7. To explain this, the deposited carbon was investigated further by TEM and SEM. According to previous reports, a minimum 7 nm metal particle diameter was required to form filamentous carbon.[44, 56] Filamentous carbon formed on 1.5Ni/S-1 due to the large Ni particles on the crystal surface (Fig. 9a), resulting in rapid deactivation of the catalyst. For 1.5Ni@Hol S-1, filamentous carbon also formed because of the large Ni particles that were not encapsulated in the hollow crystals (Fig. 9b). However, due to the high dispersion nickel particles in the cavity, coke cannot be produced on the encapsulated particles. The shells of hollow crystals also inhibit the impact of filamentous carbon on the small nickel particles in the cavities. So, despite generating 10.3 % carbon, 1.5Ni@Hol S-1 catalyst remains highly active. Though the Ni-Pt binary metal particles are sintering resistant in 1.5Ni-0.5Pt/S-1, the small particles deactivate due to carbon build-up without the protective shell (Fig. 9c). For 1.5Ni-0.5Pt@Hol S-1, the high dispersion and protection of shell lead to almost no coke build-up after reacting for 6 hours (Fig. 9d). The characterization results from SEM agree with these from TEM (Fig. 10).

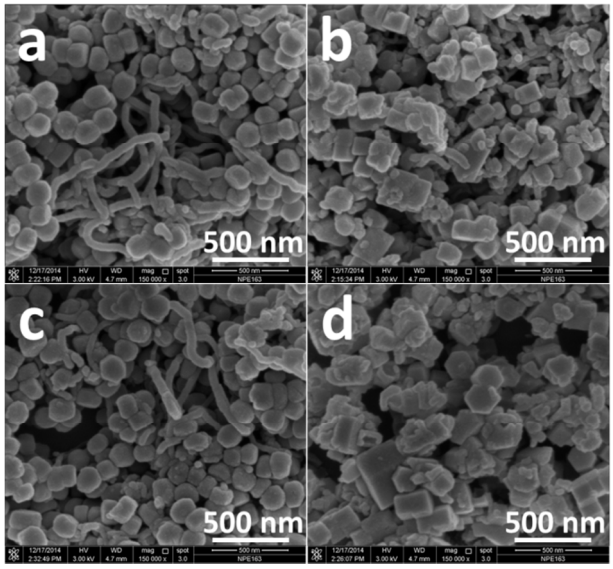

Fig. 10. SEM images of the spent catalysts, (a) 1.5Ni/S-1, (b) 1.5Ni@Hol S-1, (c) 1.5Ni-0.5Pt/S-1, (d) 1.5Ni-0.5Pt@Hol S-1, the reaction time was 1 h for 1.5Ni/S-1 and 6 h for the other three catalysts.

4 Conclusions

Ni-Pt binary metal nanoparticles with a small average size of 4.57 nm have been successfully encapsulated in hollow silicalite-1 single crystals. Compared with single metals (Ni or Pt) in the hollow crystals, 1.5Ni-0.5Pt@Hol S-1 enhances the dispersion of nickel and platinum. Meanwhile, the

encapsulation process enhances the interaction between nickel, platinum and support; making the catalyst sintering and coking resistant in dry (CO_2) reforming of CH_4.

The present work provides a general and robust strategy to prepare coke resistant catalysts for dry reforming of CH_4 and multi-metallic catalysts with well-dispersed nanoparticles.

Author contribute

C. Y. Dai and S. H. Zhang contributed equally.

Notes and references

[a]State Key Laboratory of Fine Chemicals, PSU-DUT Joint Center for Energy Research, School of Chemical Engineering, Dalian University of Technology, Dalian 116024, P. R. China. Fax: +86-0411-84986134; Tel: +86-0411-84986133, +86-0411-84986134; E-mail: guoxw@dlut.edu.cn
[b]Laboratory of Plasma Physical Chemistry, Dalian University of Technology, Dalian 116024, P. R. China. Tel: +86-0411-84986083; E-mail: chuanshi@dlut.edu.cn
[c]EMS Energy Institute, PSU-DUT Joint Center for Energy Research, Department of Energy & Mineral Engineering, and Department of Chemical Engineering Pennsylvania State University, University Park, Pennsylvania 16802, United States. Fax: 814-865-3573; Tel: 814-863-4466; E-mail: csong@psu.edu

†Electronic Supplementary Information (ESI) available: [XRD patterns, metal particle size distributions of prepared samples, ^{29}Si MAR NMR spectra, FT-IR spectra, effect of reaction temperature and Ni, Pt contents on CH_4 and CO_2 conversions over the catalysts].

1 D. Pakhare and J. Spivey, *Chem. Soc. Rev.*, 2014, **43**, 7813-7837.
2 C. J. Liu, J. Y. Ye, J. J. Jiang and Y. X. Pan, *ChemCatChem*, 2011, **3**, 529-541.
3 C. S. Song, *Catal. Today*, 2006, **115**, 2-32.
4 J. H. Edwards and A. M. Maitra, *Fuel Process. Technol.*, 1995, **42**, 269-289.
5 A. Wörner and R. Tamme, *Catal. Today*, 1998, **46**, 165-174.
6 S. Wang, G. Lu and G. J. Millar, *Energy Fuels*, 1996, **10**, 896-904.
7 A. Peters, F. Nouroozi, D. Richter, M. Lutecki and R. Glaser, *ChemCatChem*, 2012, **3**, 598−606.
8 L. Xu, H. Song and L. Chou, *ACS Catal*., 2012, **2**, 1331-1342.
9 A. Djaidja, S. Libs, A. Kiennemann and A. Barama, *Catal. Today*, 2006, **113**, 194-200.
10 M. Fan, A. Z. Abdullah and S. Bhatia, *ChemSusChem*, 2011, **4**, 1643-1653.
11 N. Sun, X. Wen, F. Wang, W. Wei and Y. Sun, *Energy Environ. Sci.*, 2010, **3**, 366-369.
12 J. Wei and E. Iglesia, *J. Catal.*, 2004, **224**, 370-383.
13 S. Tang, L. Ji, J. Lin, H. C. Zeng, K. L. Tan and K. Li, *J. Catal.*, 2000, **194**, 424-430.
14 V. M. Gonzalez-Delacruz, J. P. Holgado, R. Pereniguez and A. Caballero, *J. Catal.*, 2008, **257**, 307-314.
15 J. Ashok and S. Kawi, *Int. J. Hydrogen Energy*, 2013, **38**, 13938-13949.
16 J. Ashok and S. Kawi, *ACS Catal.*, 2013, **4**, 289-301.
17 J. Ashok, M. Subrahmanyam and A. Venugopal, *Int. J. Hydrogen Energy*, 2008, **33**, 2704-2713.
18 Z. Hou, J. Gao, J. Guo, D. Liang, H. Lou and X. Zheng, *J. Catal.*, 2007, **250**, 331-341.
19 J. Zhang, H. Wang and A. K. Dalai, *Appl. Catal., A*, 2008, **339**, 121-129.
20 J. S. Chang, S. E. Park and H. Z. Chon, *Appl. Catal. A*, 1996, **145**, 111-124.
21 J. Juan-Juan, M. C. Roman-Martinez and M. J. Illan-Gomez, *Appl. Catal. A*, 2006, **301**, 9-15.
22 A. A. Lemonidou and I. A. Vasalos, *Appl. Catal. A*, 2002, **228**, 227-235.
23 T. Osaki and T. Mori, *J. Catal.*, 2001, **204**, 89-97.
24 V. C. H. Kroll, H. M. Swaan, S. Lacombe and C. Mirodatos, *J. Catal.*, 1996, **164**, 387-398.
25 N. Wang, K. Shen, L. Huang, X. Yu, W. Qian and W. Chu, *ACS Catal.*, 2013, **3**, 1638-1651.
26 S. Damyanova, B. Pawelec, K. Arishtirova, J. L. G. Fierro, C. Sener and T. Dogu, *Appl. Catal. B*, 2009, **92**, 250-261.
27 M. García-DiØguez, I. S. Pieta, M. C. Herrera, M. A. Larrubia and L. J. Alemany, *J. Catal.*, 2010, **270**, 136-145.
28 L. Guczi, G. Stefler, O. Geszti, I. Sajo, Z. Paszti, A. Tompos and Z. Schay, *Appl. Catal. A*, 2010, **375**, 236-246.
29 S. A. Theofanidis, V. V. Galvita, H. Poelman and G. B. Marin, *ACS Catal.*, 2015, **5**, 3028-3039.
30 D. Baudouin, K. C. Szeto, P. Laurent, A. D. Mallmann, B. Fenet, L. Veyre, U. Rodemerck, C. Copeŕet and C. Thieuleux, *J. Am. Chem. Soc.*, 2012, **134**, 20624-20627.
31 P. Frontera, A. Aloise, A. Macario, F. Crea, P. L. Antonucci, G. Giordano and J. B. Nagy, *Res. Chem. Intermed.*, 2011, **37**, 267-279.
32 K.-M. Kang, H.-W. Kim, I.-W. Shim and H.-Y. Kwak, *Fuel Process. Technol.*, 2011, **92**, 1236-1243.
33 H.-W. Kim, K.-M. Kang, H.-Y. Kwak and J. H. Kim, *Chem. Eng. J.*, 2011, **168**, 775-783.
34 M. García-Diéguez, E. Finocchio, M. Á. Larrubia, L. J. Alemany and G. Busca, *J. Catal.*, 2010, **274**, 11-20.
35 X. P. Yu, F. B. Zhang, N. Wang, S. X. Hao and W. Chu, *Catal. Lett.*, 2014, **144**, 293-300.
36 K. Nagaoka, A. Jentys and J. A. Lercher, *J. Catal.*, 2005, **229**, 185-196.
37 L. Li, Y. Yao, B. Sun, Z. Fei, H. Xia, J. Zhao, W. Ji and C. T. Au, *ChemCatChem*, 2013, **5**, 3781-3787.
38 Z. W. Li, L. Y. Mo, Y. Kathiraser and S. Kawi, *ACS Catal*., 2014, **4**, 1526-1536.
39 T. Montini, A. M. Condò, N. Hickey, F. C. Lovey, L. De Rogatis, P. Fornasiero and M. Graziani, *Appl. Catal., B*, 2007, **73**, 84-97.
40 A. Corma, *Chem. Rev.*, 1997, **97**, 2373-2419.
41 X. F. Qian, B. Li, Y. Y. Hu, G. X. Niu, D. Y. Zhang, R. C. Che, Y. Tang, D. S. Su, A. M. Asiri and D. Y. Zhao, *Chem. Eur. J.*, 2012, **18**, 931-939.
42 D. Verboekend, R. Caicedo-Realpe, A. Bonilla, M. Santiago and J. Pérez-Ramírez, *Chem. Mater.*, 2010, **22**, 4679-4689.
43 C. Dai, A. Zhang, L. Li, K. Hou, F. Ding, J. Li, D. Mu, C. Song, M. Liu and X. Guo, *Chem. Mater.*, 2013, **25**, 4197-4205.
44 S. Li, L. Burel, C. Aquino, A. Tuel, F. Morfin, J. L. Rousset and D. Farrusseng, *Chem. Commun.*, 2013, **49**, 8507-8509.

45 N. Ren, Y. Yang, Y. Zhang, Q. Wang and Y. Tang, *J. Catal.*, 2007, **246**, 215-222.
46 C. Dai, A. Zhang, J. Li, K. Hou, M. Liu, C. Song and X. Guo, *Chem. Commun.*, 2014, **50**, 4846-4848.
47 S. Li, A. Tuel, D. Laprune, F. Meunier and D. Farrusseng, *Chem. Mater.*, 2015, **27**, 276-282.
48 C. Dai, X. Li, A. Zhang, C. Liu, C. Song and X. Guo, *RSC Adv.*, 2015, **5**, 40297-40302.
49 K. Sadowska, A. Wach, Z. Olejniczak, P. Kuśtrowski and J. Datka, *Micropor. and Mesopor. Mater.*, 2013, **167**, 82-88.
50 N. Wang, K. Shen, X. Yu, W. Qian and W. Chu, *Catal. Sci. Technol.*, 2013, **3**, 2278-2287.
51 T. Xie, L. Y. Shi, J. P. Zhang and D. S. Zhang, *Chem. Commun.*, 2014, **50**, 7250-7253.
52 A. Horváth, G. Stefler, O. Geszti, A. Kienneman, A. Pietraszek and L. Guczi, *Catal. Today*, 2011, **169**, 102-111.
53 H. Kan and H. Lee, *Appl. Catal. B*, 2010, **97**, 108-114.
54 Y. X. Pan, C. J. Liu and L. Cui, *Catal. Lett.*, 2008, **123**, 96-101.
55 J. W. Han, C. Kim, J. S. Park and H. Lee, *ChemSusChem*, 2014, **7**, 451-456.
56 J. H. Kim, D. J. Suh, T. J. Park and K. L. Kim, *Appl. Catal. A*, 2000, **197**, 191-200.